Integrated optical frequency shifter in silicon-organic hybrid (SOH) technology

M. Lauermann,[1] C. Weimann,[1] A. Knopf,[2] W. Heni,[1,6] R. Palmer,[1,7] S. Koeber,[1,5,8] D. L. Elder,[3] W. Bogaerts,[4] J. Leuthold,[1,6] L. R. Dalton,[3] C. Rembe,[2,9] W. Freude,[1] and C. Koos[1,5,*]

[1] *Karlsruhe Institute of Technology, Institute of Photonics and Quantum Electronics, 76131 Karlsruhe, Germany*
[2] *Polytec GmbH, 76337 Waldbronn, Germany*
[3] *University of Washington, Department of Chemistry, Seattle, WA 98195-1700, United States*
[4] *Ghent University – IMEC, Photonics Research Group, Gent, Belgium*
[5] *Karlsruhe Institute of Technology, Institute of Microstructure Technology 76344 Eggenstein-Leopoldshafen, Germany*
[6] *Now with: Institute of Electromagnetic Fields, ETH Zurich, Zurich, Switzerland*
[7] *Now with: Coriant GmbH, 81541 Munich, Germany*
[8] *Now with: University of Cologne, Chemistry Department, 50939 Cologne, Germany*
[9] *Now with: Clausthal University of Technology, Institute of Electrical Information Technology, 38678 Clausthal-Zellerfeld, Germany.*
*christian.koos@kit.edu

Abstract: We demonstrate for the first time a waveguide-based frequency shifter on the silicon photonic platform using single-sideband modulation. The device is based on silicon-organic hybrid (SOH) electro-optic modulators, which combine conventional silicon-on-insulator waveguides with highly efficient electro-optic cladding materials. Using small-signal modulation, we demonstrate frequency shifts of up to 10 GHz. We further show large-signal modulation with optimized waveforms, enabling a conversion efficiency of -5.8 dB while suppressing spurious side-modes by more than 23 dB. In contrast to conventional acousto-optic frequency shifters, our devices lend themselves to large-scale integration on silicon substrates, while enabling frequency shifts that are several orders of magnitude larger than those demonstrated with all-silicon serrodyne devices.

OCIS codes: (250.4110) Modulators; (060.2630) Frequency modulation.

References and links

1. M. P. Kothiyal and C. Delisle, "Optical frequency shifter for heterodyne interferometry using counterrotating wave plates," Opt. Lett. **9**, 319 (1984).
2. M. Bauer, F. Ritter, and G. Siegmund, "High-precision laser vibrometers based on digital Doppler signal processing," in E. P. Tomasini, ed. (2002), pp. 50–61.
3. Y. Ma, Q. Yang, Y. Tang, S. Chen, and W. Shieh, "1-Tb/s single-channel coherent optical OFDM transmission over 600-km SSMF fiber with subwavelength bandwidth access," Optics Express **17**, 9421 (2009).
4. R. Watts, S. G. Murdoch, and L. Barry, "Spectral linewidth reduction of single-mode and mode-locked lasers using a feed-forward heterodyne detection scheme," in *CLEO: 2014* (OSA, 2014), p. STh3O.8.
5. J. S. Orcutt, B. Moss, C. Sun, J. Leu, M. Georgas, J. Shainline, E. Zgraggen, H. Li, J. Sun, M. Weaver, S. Urošević, M. Popović, R. J. Ram, and V. Stojanović, "Open foundry platform for high-performance electronic-photonic integration," Opt. Express **20**, 12222 (2012).
6. M. Hochberg, N. C. Harris, Ran Ding, Yi Zhang, A. Novack, Zhe Xuan, and T. Baehr-Jones, "Silicon photonics: The next fabless semiconductor industry," IEEE Solid State Circuits Mag. **5**, 48–58 (2013).
7. R. G. Hunsperger, *Integrated Optics: Theory and Technology*, 6th ed, Advanced Texts in Physics (Springer, 2009).
8. Y. Park and K. Cho, "Heterodyne interferometer scheme using a double pass in an acousto-optic modulator," Opt. Lett. **36**, 331 (2011).
9. L. M. Johnson and C. H. Cox, "Serrodyne optical frequency translation with high sideband suppression," J. Lightw. Technol. **6**, 109–112 (1988).
10. M. Izutsu, S. Shikama, and T. Sueta, "Integrated optical SSB modulator/frequency shifter," IEEE Journal of Quantum Electronics **17**, 2225–2227 (1981).

11. Y. Li, S. Meersman, and R. Baets, "Optical frequency shifter on SOI using thermo-optic serrodyne modulation," in *Group IV Photonics (GFP)* (IEEE, 2010), pp. 75–77.
12. Y. Li, S. Verstuyft, G. Yurtsever, S. Keyvaninia, G. Roelkens, D. Van Thourhout, and R. Baets, "Heterodyne laser Doppler vibrometers integrated on silicon-on-insulator based on serrodyne thermo-optic frequency shifters," Applied Optics **52**, 2145 (2013).
13. G. T. Reed, G. Mashanovich, F. Y. Gardes, and D. J. Thomson, "Silicon optical modulators," Nature Photon. **4**, 518–526 (2010).
14. G. Cocorullo and I. Rendina, "Thermo-optical modulation at 1.5μm in silicon etalon," Electron. Lett. **28**, 83–85 (1992).
15. S. Shimotsu, S. Oikawa, T. Saitou, N. Mitsugi, K. Kubodera, T. Kawanishi, and M. Izutsu, "Single side-band modulation performance of a $LiNbO_3$ integrated modulator consisting of four-phase modulator waveguides," IEEE Photonics Technology Letters **13**, 364–366 (2001).
16. C. Koos, J. Leuthold, W. Freude, M. Kohl, L. Dalton, W. Bogaerts, A. Giesecke, M. Lauermann, A. Melikyan, S. Koeber, S. Wolf, C. Weimann, S. Muehlbrandt, K. Koehnle, J. Pfeifle, W. Hartmann, Y. Kutuvantavida, S. Ummethala, R. Palmer, D. Korn, L. Alloatti, P. Schindler, D. Elder, T. Wahlbrink, and J. Bolten, "Silicon-organic hybrid (SOH) and plasmonic-organic hybrid (POH) integration," J. Lightw. Technol. **34**, 256–268 (2016).
17. S. Koeber, R. Palmer, M. Lauermann, W. Heni, D. L. Elder, D. Korn, M. Woessner, L. Alloatti, S. Koenig, P. C. Schindler, H. Yu, W. Bogaerts, L. R. Dalton, W. Freude, J. Leuthold, and C. Koos, "Femtojoule electro-optic modulation using a silicon–organic hybrid device," Light Sci. Appl. **4**, e255 (2015).
18. T. Baehr-Jones, M. Hochberg, G. Wang, R. Lawson, Y. Liao, P. A. Sullivan, L. Dalton, A. K.-Y. Jen, and A. Scherer, "Optical modulation and detection in slotted silicon waveguides," Opt. Express **13**, 5216 (2005).
19. J. Pfeifle, L. Alloatti, W. Freude, J. Leuthold, and C. Koos, "Silicon-organic hybrid phase shifter based on a slot waveguide with a liquid-crystal cladding," Opt. Express **20**, 15359 (2012).
20. Y. Xing, T. Ako, J. P. George, D. Korn, H. Yu, P. Verheyen, M. Pantouvaki, G. Lepage, P. Absil, A. Ruocco, C. Koos, J. Leuthold, K. Neyts, J. Beeckman, and W. Bogaerts, "Digitally controlled phase shifter using an SOI slot waveguide with liquid crystal infiltration," IEEE Photon. Technol. Lett. **27**, 1269–1272 (2015).
21. D. Korn, M. Lauermann, S. Koeber, P. Appel, L. Alloatti, R. Palmer, P. Dumon, W. Freude, J. Leuthold, and C. Koos, "Lasing in silicon–organic hybrid waveguides," Nature Communications **7**, 10864 (2016).
22. F. Qiu, H. Sato, A. M. Spring, D. Maeda, M. Ozawa, K. Odoi, I. Aoki, A. Otomo, and S. Yokoyama, "Ultra-thin silicon/electro-optic polymer hybrid waveguide modulators," Applied Physics Letters **107**, 123302 (2015).
23. V. R. Almeida, Q. Xu, C. A. Barrios, and M. Lipson, "Guiding and confining light in void nanostructure," Opt. Lett. **29**, 1209 (2004).
24. S. Inoue and A. Otomo, "Electro-optic polymer/silicon hybrid slow light modulator based on one-dimensional photonic crystal waveguides," Applied Physics Letters **103**, 171101 (2013).
25. X. Zhang, A. Hosseini, S. Chakravarty, J. Luo, A. K.-Y. Jen, and R. T. Chen, "Wide optical spectrum range, subvolt, compact modulator based on an electro-optic polymer refilled silicon slot photonic crystal waveguide," Opt. Lett. **38**, 4931 (2013).
26. M. Gould, T. Baehr-Jones, R. Ding, S. Huang, J. Luo, A. K.-Y. Jen, J.-M. Fedeli, M. Fournier, and M. Hochberg, "Silicon-polymer hybrid slot waveguide ring-resonator modulator," Opt. Express **19**, 3952 (2011).
27. M. Lauermann, C. Weimann, A. Knopf, D. L. Elder, W. Heni, R. Palmer, D. Korn, P. Schindler, S. Koeber, L. Alloatti, H. Yu, W. Bogaerts, L. R. Dalton, C. Rembe, J. Leuthold, W. Freude, and C. Koos, "Integrated Silicon-Organic Hybrid (SOH) Frequency Shifter," in (Optical Fiber Communication Conference, 2014), p. Tu2A.1.
28. R. Palmer, L. Alloatti, D. Korn, W. Heni, P. C. Schindler, J. Bolten, M. Karl, M. Waldow, T. Wahlbrink, W. Freude, C. Koos, and J. Leuthold, "Low-loss silicon strip-to-slot mode converters," IEEE Photon. J. **5**, 2200409–2200409 (2013).
29. D. Vermeulen, S. Selvaraja, P. Verheyen, G. Lepage, W. Bogaerts, P. Absil, D. Van Thourhout, and G. Roelkens, "High-efficiency fiber-to-chip grating couplers realized using an advanced CMOS-compatible silicon-on-insulator platform," Opt. Express **18**, 18278 (2010).
30. D. Benedikovic, C. Alonso-Ramos, P. Cheben, J. H. Schmid, S. Wang, D.-X. Xu, J. Lapointe, S. Janz, R. Halir, A. Ortega-Moñux, J. G. Wangüemert-Pérez, I. Molina-Fernández, J.-M. Fédéli, L. Vivien, and M. Dado, "High-directionality fiber-chip grating coupler with interleaved trenches and subwavelength index-matching structure," Optics Letters **40**, 4190 (2015).
31. N. Lindenmann, S. Dottermusch, M. L. Goedecke, T. Hoose, M. R. Billah, T. P. Onanuga, A. Hofmann, W. Freude, and C. Koos, "Connecting silicon photonic circuits to multicore fibers by photonic wire bonding," J. Lightw. Technol. **33**, 755–760 (2015).
32. R. Palmer, S. Koeber, D. Elder, M. Woessner, W. Heni, D. Korn, M. Lauermann, W. Bogaerts, L. Dalton, W. Freude, J. Leuthold, and C. Koos, "High-speed, low drive-voltage silicon-organic hybrid modulator based on a binary-chromophore electro-optic material," J. Lightw. Technol. **32**, 2726–2734 (2014).
33. J. Witzens, T. Baehr-Jones, and M. Hochberg, "Design of transmission line driven slot waveguide Mach-Zehnder interferometers and application to analog optical links," Opt. Express **18**, 16902 (2010).
34. L. Alloatti, M. Lauermann, C. Sürgers, C. Koos, W. Freude, and J. Leuthold, "Optical absorption in silicon layers in the presence of charge inversion/accumulation or ion implantation," Appl. Phys. Lett. **103**, 051104 (2013).

35. X. Zhang, C. Chung, A. Hosseini, H. Subbaraman, J. Luo, A. Jen, R. Neilson, C. Lee, and R. T. Chen, "High performance optical modulator based on electro-optic polymer filled silicon slot photonic crystal waveguide," J. Lightw. Technol. 1–1 (2015).
36. L. Alloatti, D. Korn, R. Palmer, D. Hillerkuss, J. Li, A. Barklund, R. Dinu, J. Wieland, M. Fournier, J. Fedeli, H. Yu, W. Bogaerts, P. Dumon, R. Baets, C. Koos, W. Freude, and J. Leuthold, "42.7 Gbit/s electro-optic modulator in silicon technology," Opt. Express **19**, 11841 (2011).
37. W. Hartmann, M. Lauermann, S. Wolf, H. Zwickel, Y. Kutuvantavida, J. Luo, A. K.-Y. Jen, W. Freude, and C. Koos, "100 Gbit/s OOK using a silicon-organic hybrid (SOH) modulator," in *European Conference on Optical Communication (ECOC), 2015* (IEEE, 2015), p. PDP.1.4.
38. D. L. Elder, S. J. Benight, J. Song, B. H. Robinson, and L. R. Dalton, "Matrix-assisted poling of monolithic bridge-disubstituted organic NLO chromophores," Chem. Mat. **26**, 872–874 (2014).
39. M. Lauermann, S. Wolf, P. C. Schindler, R. Palmer, S. Koeber, D. Korn, L. Alloatti, T. Wahlbrink, J. Bolten, M. Waldow, M. Koenigsmann, M. Kohler, D. Malsam, D. L. Elder, P. V. Johnston, N. Phillips-Sylvain, P. A. Sullivan, L. R. Dalton, J. Leuthold, W. Freude, and C. Koos, "40 GBd 16QAM signaling at 160 Gb/s in a silicon-organic hybrid modulator," J. Lightw. Technol. **33**, 1210–1216 (2015).
40. L. Alloatti, R. Palmer, S. Diebold, K. P. Pahl, B. Chen, R. Dinu, M. Fournier, J.-M. Fedeli, T. Zwick, W. Freude, C. Koos, and J. Leuthold, "100 GHz silicon–organic hybrid modulator," Light Sci. Appl. **3**, e173 (2014).
41. Z. Shi, W. Liang, J. Luo, S. Huang, B. M. Polishak, X. Li, T. R. Younkin, B. A. Block, and A. K.-Y. Jen, "Tuning the kinetics and energetics of Diels−Alder cycloaddition reactions to improve poling efficiency and thermal stability of high-temperature cross-linked electro-optic polymers," Chem. Mat. **22**, 5601–5608 (2010).
42. L. R. Dalton, P. A. Sullivan, and D. H. Bale, "Electric field poled organic electro-optic materials: state of the art and future prospects," Chem. Rev. **110**, 25–55 (2010).
43. J. Luo, S. Huang, Z. Shi, B. M. Polishak, X.-H. Zhou, and A. K. Jen, "Tailored organic electro-optic materials and their hybrid systems for device applications," Chem. Mat. **23**, 544–553 (2011).
44. J. P. Salvestrini, L. Guilbert, M. Fontana, M. Abarkan, and S. Gille, "Analysis and control of the DC drift in LiNbO3-based Mach-Zehnder modulators," J. Lightw. Technol. **29**, 1522–1534 (2011).
45. I. S. Gradshteyn and I. M. Ryzhik, *Tables of Series, Products, and Integrals*, 2nd ed. (Harri Deutsch, 1981).

1. Introduction

Frequency shifters are key elements for a wide range of applications, comprising, e.g., heterodyne interferometry, vibrometry, distance metrology, or optical data transmission [1–4]. All of these applications can benefit greatly from photonic integration, which allows to realize optical systems with high technical complexity while maintaining robustness, small footprint and low cost. Silicon photonics is a particularly attractive platform for optical integration, leveraging large-scale high-yield CMOS processing and offering the potential of co-integrating photonic and electronic devices on a common substrate [5]. Driven by applications in optical communications, a variety of foundry services have emerged over the last years offering process design kits (PDK) and libraries of standardized silicon photonic devices such as passive components, electro-optic modulators, and Germanium-based photodetectors [6]. High-performance frequency shifters, however, are still missing in the portfolio, especially when it comes to devices that combine high conversion efficiency (CE) between the original and the frequency-shifted signal with a high side-mode suppression ratio (SMSR) of the original carrier and the spurious side modes relative to the shifted spectral line.

Conventionally, frequency shifters have been realized with acousto-optic modulators (AOM), exploiting the Doppler shift of an optical wave that is scattered from a propagating sound wave [7]. When aligned for perfect phase matching, AOM provide both high SMSR and CE. However, the alignment is delicate and needs to be distinctively linked to the desired frequency shift. In addition, AOM are based on free-space optical assemblies of conventional high-precision optomechanical components [8], making the devices bulky, expensive, and sensitive to vibrations and environmental influences. Moreover, AOM require material systems with strong acousto-optic and ideally also piezoelectric effects, ruling out silicon as an integration platform by fundamental principles. AOM-based systems are hence inherently unsuited for integration on the silicon platform.

Alternatively, waveguide-based frequency shifters can be used, exploiting either the so-called serrodyne technique [9] or single-sideband modulation in an in-phase/quadrature (IQ) modulator [10]. For serrodyne modulation, an electro-optic phase shifter is driven by a

sawtooth signal with a peak-to-peak drive amplitude that leads exactly to a 2π phase shift of the optical carrier. This results in a phase shift that is piecewise linear in time and hence leads to a frequency shift that corresponds to the fundamental frequency of the sawtooth drive signal. Such devices have been demonstrated on the silicon photonic platform, providing a remarkable SMSR of 39 dB [11,12], but the achievable frequency shift is limited by fundamental properties of silicon-based phase shifters: To avoid unwanted spurious lines in the output spectrum, pure serrodyne phase modulation must be achieved without any residual amplitude modulation. This cannot be accomplished by using conventional silicon photonic phase shifters that rely on injection or depletion of free carriers in reverse or forward-biased p-n or p-i-n junctions [13]. Instead, thermo-optic phase modulators had to be used, leading to stringent limitations of the achievable frequency shift. In particular, a good SMSR requires a perfect sawtooth-like phase shift that contains a large number of higher-order harmonics besides the fundamental frequency component [9]. Given the time constants and the associated bandwidth limitations of thermo-optic phase shifters [14], this is possible for very small fundamental frequencies only, thereby limiting the achievable frequency shifts to values of, e.g., 10 kHz [11], which is insufficient for many applications. In the case of single-sideband (SSB) modulation, two Mach-Zehnder modulators (MZM) are combined with a $\pi/2$ phase shift to form an optical IQ modulator [10]. Both MZM are biased in the zero-transmission point. The in-phase (I) and quadrature (Q) MZM are driven with a sine signal and cosine signal, respectively, which, in the small-signal regime, leads to a frequency shift that corresponds to the frequency of the sinusoidal drive signals. As for the serrodyne method, a good SMSR requires a pure frequency shift without any spurious amplitude-phase coupling, making it challenging to realize high-performance single-sideband modulators based on the standard silicon photonic device portfolio. Previous demonstrations of integrated optical SSB frequency shifters are therefore limited to the $LiNbO_3$ platform [15], which is not suited for large-scale photonic integration and needs high drive voltages of more than 6 V_{pp}. Moreover, conventional SSB modulation suffers from a trade-off between SMSR and CE: For high SMSR, the MZM need to be driven in the small-signal regime, where the amplitude transmission is proportional to the applied voltage. This leads to large modulation loss and hence small CE. High CE, on the other hand, would require large signals to drive the device to maximum transmission, thereby inducing spurious side-modes in the optical spectrum due to the nonlinear transfer function of the MZM [15].

In this paper we demonstrate the first single-sideband (SSB) frequency shifter based on silicon photonic waveguides. We exploit the silicon-organic hybrid (SOH) integration concept to realize broadband phase shifters that feature low drive voltages and enable pure phase modulation. SOH integration allows to combine conventional silicon-on-insulator (SOI) waveguides with a wide variety of organic cladding materials and has been used to realize efficient electro-optic modulators [16–18], ultra-compact phase shifters [19,20], as well as lasers [21]. Interaction of the guided light with the organic cladding of the SOH device can be enhanced by using thin ultra-thin strip [22] or slot waveguides [23], which can additionally be combined with photonic crystal structures [24,25] or ring resonators [26]. In our experiments, we use conventional SOH slot-waveguide modulators to show frequency shifts of up to 10 GHz and a carrier suppression of 37 dB for the case of SSB modulation in the small-signal regime [27]. Moreover, we experimentally demonstrate temporal shaping of the drive signal to overcome the trade-off of SMSR and CE. We demonstrate a CE of -5.8 dB while maintaining a SMSR of 23.5 dB. The experimentally obtained CE is quite close to the theoretically predicted value of - 6 dB. These results are achieved with first-generation devices, leaving considerable room for further improvement.

This paper is structured as follows: In Section 2, we explain the theoretical concepts of frequency shifters based on IQ modulators. Section 3 introduces the SOH phase shifters used for realizing the frequency shifters. Section 4 describes experimental demonstrations the devices and discusses the achieved performance. A rigorous mathematical description of frequency shifters based on single-sideband modulation is given in the Appendix.

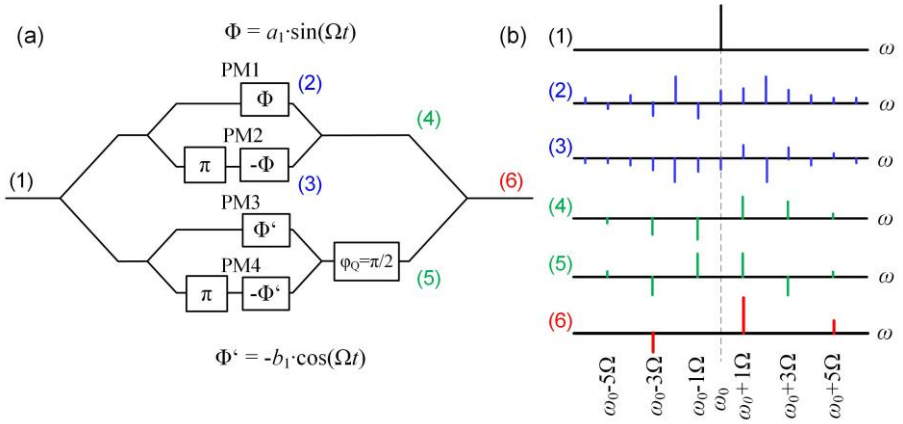

Fig. 1: IQ modulator structure for single-sideband operation. **(a)** Schematic of the modulator structure. Four phase modulators (PM 1 … 4) are paired to two Mach-Zehnder modulators (MZM). The MZM are biased in zero transmission and operated in push-pull mode with sinusoidal electrical drive signals that feature a relative phase shift of π/2. The outputs of the MZM are combined with a relative optical phase difference of π/2. **(b)** Sketch of the field amplitude spectrum at various points of the modulator structure. The spectral lines feature phases of 0 or π, which are indicated by positive or negative peak values, respectively. At the output of the frequency shifter, most of the energy has been transferred into the line which is shifted by the modulation frequency Ω. When the MZM is not driven in the small-signal regime, additional harmonics can be seen in the output spectrum. Ω represents the RF modulation frequency while ω_0 denotes the frequency of the optical carrier.

2. Frequency shifters based on IQ-modulators

The concept of SSB frequency shifting with an integrated IQ modulator was first described by Izutsu *et al.* in 1981 [10]. The general principle is explained in Fig. 1 (a): The optical input is split and fed into four phase modulators which are paired to two MZM, the output of which are combined with a relative phase shift of π/2. Both MZM are biased at zero transmission (null point), indicated by the π phase shift in the lower arm of each MZM in Fig. 1(a) and both MZM are driven in push-pull mode by a sine and cosine of angular frequency Ω, respectively. Fig. **1**(b) illustrates the optical spectra that can be found at various positions (1) … (6) in the SSB modulator setup. After one phase shifter, a multitude of spectral lines emerge in the frequency domain, separated by the modulation frequency Ω, see displays (2) and (3) in Fig. 1(b). The amplitudes of the lines depend on the modulation depth and can be described by Bessel functions, see Appendix for a detailed mathematical description. When the signals of a pair of phase shifters are combined at the output of the MZM, the spectral components at the optical carrier frequency ω_0 and all even-order side lines interfere destructively, see displays (4) and (5). Moreover, at the output of the IQ modulator, the signals from both MZM are combined with a relative phase shift of π/2, leading to a destructive interference of the lines at $\omega_0 - 1\Omega$, $\omega_0 + 3\Omega$, $\omega_0 - 5\Omega$ etc., see display (6) in Fig. 1(b). The direction of the frequency shift can be chosen arbitrarily: By assigning the π/2 phase shift to the other arm of the IQ modulator, the lines interfere constructively at $\omega_0 - 1\Omega$ instead of $\omega_0 + 1\Omega$, the output spectrum is flipped about ω_0.

For practically relevant modulation depths, the spectral line at $\omega_0 + \Omega$ carries most of the energy at the output of the frequency shifter, while unwanted side modes appear at $\omega_0 - 3\Omega$, $\omega + 5\Omega$, $\omega - 7\Omega$,... with decreasing intensity, see Appendix for a mathematical description. For small-signal modulation, i.e., for drive voltage amplitudes that are much smaller than the π-voltage of the MZM, the spurious side modes at $\omega_0 - 3\Omega$, $\omega_0 + 5\Omega$ and higher can be neglected. This can be understood intuitively when considering the field amplitude transfer function of a single MZM, which is depicted in Fig. 2 along with the corresponding output spectrum for different drive conditions. For small-signal modulation around the null point, only the linear part of the MZM field transfer function is used for modulation by the

sinusoidal drive signal, hence the amplitude modulation at the output is sinusoidal as well. This results in only two side-modes, see Fig. 2(a). Since the MZM are biased in the null-point, small-signal modulation leads to a low conversion efficiency, and most of the power is lost to the destructive port of the amplitude combiners at the output of the MZM. For large-signal modulation, in contrast, the output signal is a distorted sine, leading to larger conversion efficiency but spurious side modes, Fig. 2(b).

To achieve high conversion efficiency and high SMSR simultaneously, the drive signal has to be predistorted to suppress the spurious side modes. This can be accomplished by adding higher harmonics to the drive signal to generate new side modes which can destructively interfere with the spurious modes from the fundamental drive frequency. For example, when the third harmonic $a_3 \sin(3\Omega)$ is added to the RF drive signal, the optical amplitude at the output can be described by

$$E = E_0 e^{j\omega_0 t} \begin{pmatrix} \ldots + J_0(a_3)J_1(a_1)e^{j\Omega t} \\ + J_0(a_3)J_{-3}(a_1)e^{-j3\Omega t} - J_0(a_1)J_{-1}(a_3)e^{-j3\Omega t} \\ + J_0(a_3)J_5(a_1)e^{j5\Omega t} \\ + J_0(a_3)J_{-7}(a_1)e^{-j7\Omega t} + \ldots \end{pmatrix}, \quad (1)$$

where $\underline{E}$ is a complex amplitude factor, $J_n(a_1)$ describes the Bessel function of n-th order and a_1 (a_3) is the amplitude of the first (third) harmonic of the electrical drive signal. A derivation of this relation is explained in the Appendix. With the correct amplitude levels a_1 and a_3 for the harmonics of the drive signals, the relation $J_0(a_3)J_{-3}(a_1)e^{-j3\Omega t} = J_0(a_1)J_{-1}(a_3)e^{-j3\Omega t}$ can be fulfilled and the frequency component at $\omega_0 - 3\Omega$ can be removed from the output signal, except for the contributions including the higher-order Bessel functions $J_k(a_3)$, $|k| > 1$, which can be neglected for practical modulation depths. The same procedure can be applied to remove all other spurious side modes. Hence, using an infinite number of higher harmonics in the drive signal, we can in principle suppress all side modes and only retain the frequency-shifted component at $\omega_0 + \Omega$. For an ideal IQ modulator, the resulting drive signal would be perfectly triangular and feature an amplitude of $a_1 = \pi/2$.

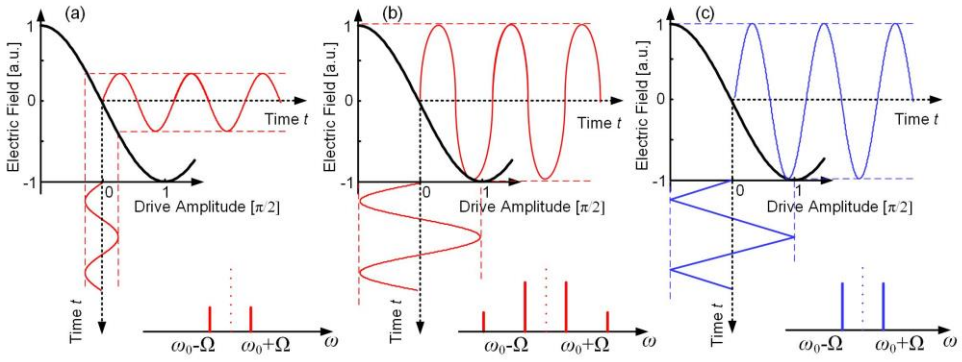

Fig. 2: Field amplitude transfer characteristics of an ideal MZM in push-pull operation along with the corresponding output spectra, the drive voltage and the electrical field at the output for different drive conditions. **(a)** Small-signal operation: The MZM is driven with a sinusoidal signal in the linear regime, resulting in two weak lines at $\omega_0 \pm \Omega$ in the output spectrum. The amplitude of the output field is relatively small, leading to a low conversion efficiency. The carrier frequency (dotted line) is only depicted for reference – it should not contain any power after the MZM, which is biased in the null point for zero transmission. **(b)** Large-signal operation with a sinusoidal drive signal. The field at the output resembles a distorted sine with large amplitude. Therefore the desired spectral lines have large intensity, but are accompanied by spurious side modes. (c) Large-signal operation with a triangular drive signal. For an ideal MZM, the output signal features a perfectly sinusoidal amplitude modulation, and the spectrum consists of only two lines at $\omega_0 \pm \Omega$. – this time with large intensity.

An intuitive illustration of this situation is again depicted in Fig. 2(c): Given the sinusoidal transfer function of the MZM, a perfectly triangular drive signal driven with amplitude $a_1 = \pi/2$ results in a sinusoidal amplitude modulation at the output, leading to only two discrete side modes at the output, one of which is annihilated by destructive interference at the output coupler of the IQ modulator. This allows realizing an ideal frequency shifter without any spurious side modes. Compared to serrodyne modulation, the sinusoidal drive signals for SSB modulation are much easier to generate than the sawtooth signal, and even the triangular drive signal has significantly less power in higher harmonic frequencies than the sawtooth signal, thereby facilitating high-bandwidth operation of the frequency shifter. Note that the preceding considerations are valid for an ideal IQ modulator, without any amplitude imbalance or phase errors. For real devices, driving the SSB modulator with a triangular signal will not necessarily lead to a perfect frequency shift. Still, the harmonics of the drive signal can be adjusted to compensate also the imperfections of the modulator.

3. Silicon-organic hybrid (SOH) frequency shifters

To avoid amplitude-phase coupling in the silicon-based modulators, the phase shifter sections are realized by silicon-organic hybrid (SOH) integration [16]. A cross section of an SOH MZM is depicted in Fig. 3(a). Each phase shifter consists of a 1.5 mm long silicon slot waveguide (w_{slot} = 140 nm, w_{rail} = 220 nm, h_{Rail} = 220 nm) with an electro-optic organic material as cladding. The device is operated in quasi-TE polarization at a wavelength of 1540 nm. Light is coupled to the chip via grating couplers and routed to the frequency shifter via standard SOI strip waveguides. Multimode interference coupler (MMI) are used as power splitter and combiner. To couple the light into the slot waveguide, optimized logarithmic tapers are used [28]. The fiber-to-fiber loss of the device amounts to 29 dB when tuning the modulator to max. transmission. This rather high excess loss is dominated by the coupling loss of the two grating coupler with approx. 6 dB, each. The 7 mm long access waveguides add 0.6 dB/mm loss due to sidewall roughness. The optimized strip-to-slot converters and MMI have an aggregate loss of less than 2 dB. The 1.5 mm long active slot waveguide is estimated to have a loss of 7.3 dB/mm. The overall insertion loss of the frequency shifter can be reduced considerably in future device generations:

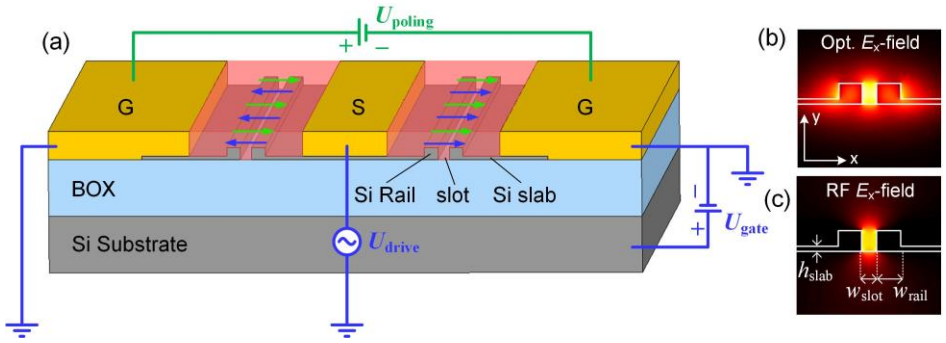

Fig. 3(a): Cross-sectional view of a SOH MZM. The slot waveguides are filled with the electro-optic organic material DLD164. Electrical contact to the ground-signal-ground (GSG) transmission line of the MZM is established by thin *n*-doped silicon slabs. The EO material in the slot is poled via a DC poling voltage U_{poling} applied to the floating ground electrodes of the MZM, and the electro-optic chromophores in both arms orient along the electrical field in the same direction as indicated by green arrows. For operation of the device, an RF signal is fed to the GSG electrodes. The associated electric field, indicated by blue arrows, is parallel to the poling direction in the right arm, and antiparallel in the left arm. This leads to phase shifts of equal magnitude but opposite sign and hence to push-pull operation of the MZM. A static gate voltage U_{gate} is applied between the substrate and the device layer to increase the conductivity of the silicon slab. **(b)** Dominant E_x component of the optical field and **(c)** E_x component of the electrical drive signal in the slot waveguide. Both fields are confined to the slot and overlap strongly within the EO material, thereby enabling efficient phase shifting.

The loss of the undoped slot waveguides can be reduced to 1 dB/mm [29], optimized grating couplers and photonic wire bonds are available with losses below 2 dB [30,31]. Using slot waveguides with improved doping profiles the propagation loss in the modulator section can be reduced to below 1.5 dB/mm, leading to an overall fiber-to-fiber loss below 10 dB. When operating the waveguide in quasi-TE polarization, the high index contrast between the silicon rails (n = 3.48) and the organic cladding (n = 1.83) leads to an enhanced optical field in the slot. A thin n-doped silicon slab electrically connects the rails to ground-signal-ground (GSG) travelling-wave electrodes. The modulation RF voltage applied to the electrodes drops predominantly over the narrow slot, leading to a strong modulating RF field, which overlaps with the optical quasi-TE mode. This leads to highly efficient phase modulation. As a figure of merit for the overlap, the field confinement factor Γ is defined by the fraction of the optical field which interacts with the modulation field [32,33]. For our device the field confinement factor amounts to $\Gamma = 0.24$. The modulation efficiency of SOH devices can be increased by using a narrower slot, which leads to an increased field confinement factor and at the same time leads to a higher modulation field for a given drive voltage. We chose here a slot width of w_{slot} = 140 nm as a compromise between decent modulation efficiency and reliable fabrication using deep UV (DUV) lithography. A detailed discussion on the influence of the waveguide dimensions on the field confinement factor can be found in [16]. A gate voltage applied between the SOI substrate and the device layer can be used to induce an electron accumulation layer at the oxide-silicon interface, thereby increasing the conductivity of the silicon slabs [34,35]. In our experiment, the gate field is applied across the 2 µm thick buried oxide (BOX), which leads to a rather high voltage of 300 V to achieve a field strength of 0.15 V/nm. Using gate contacts on top of the silicon slab, the voltages can be reduced to less than 3 V [36]. For optimized doping profiles, the gate voltage can even be omitted completely – we could recently demonstrate high-speed operation of an SOH MZM operating at 80 Gbit/s without any applied gate voltage [37]. The optical cladding material consists of the strongly electro-optic chromophore DLD164 [17,38], which allows for pure phase modulation of the optical signal.The material is deposited by spin coating from 1,1,2-trichloroethane onto pre-fabricated SOI waveguide structures and dried in vacuum. To align the organic molecules, a poling process is used during fabrication: The device is heated to the glass transition temperature of 66 °C of the organic material, and a poling voltage is applied via the floating ground electrodes of each MZM. This results in a poling field of approximately 280 V/µm in each slot waveguide. The dipolar chromophore molecules hence align in the same direction as defined by the electric field, indicated by the green arrows in Fig. 3(a). After alignment, the sample is cooled down to preserve the alignment of the chromophores, and the poling voltage is removed. Using DLD164, a voltage-length product of $U_\pi L$ = 0.5 Vmm is achieved, corresponding to an in-device electro-optic coefficient of r_{33} = 150 pm/V and a poling efficiency of 0.54 cm^2/V^2. The in-device r_{33} of the SOH devices is higher than the electro-optic coefficient of r_{33} = 137 pm/V achieved for thin film experiments with bulk material, for which poling voltages were limited by dielectric breakdown [38]. Those findings are in line with previous investigations where a high in-device electro-optic coefficient of up to r_{33} = 180 pm/V was achieved [17]. For operating the device, an RF signal is coupled to the GSG transmission line, leading to a modulating electric RF field as indicated by blue arrows in Fig. 3(a). The RF field and the chromophore orientation are antiparallel to each other in the left half of the GSG transmission line, and parallel in the right half. This leads to phase shifts of opposite sign in the two arms of the MZM and hence to push-pull modulation.

4. Experimental demonstration

The setup used for experimental demonstration of the phase shifter is sketched in Fig. 4. A tunable laser is coupled to the silicon chip via grating couplers. On the chip, two SOH MZM are nested to form an IQ configuration. An intentional length imbalance of 40 µm is introduced between the two arms that contain the MZM such that the 90° phase shift between I and Q component can be adjusted by wavelength tuning. The electrical drive signal is fed to the chip via microwave probes, and the device is biased at the null point via bias-Ts.

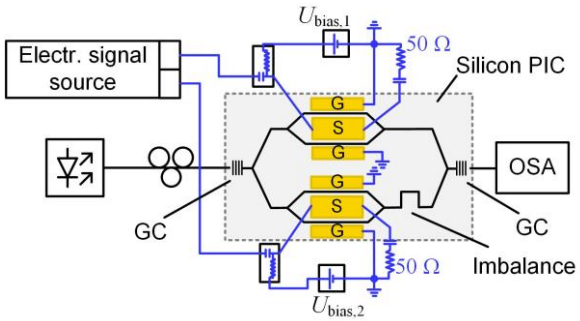

Fig. 4: Sketch of the measurement setup. A tunable laser is used as an optical source and coupled to the silicon photonic integrated circuit (PIC) via a grating coupler (GC). The PIC consists of two SOH MZM that are nested in an IQ configuration. An intentional imbalance of 40 µm is inserted between the two MZM to enable phase adjustment via wavelength tuning. For small-signal modulation with a purely sinusoidal electrical drive signal, we use a radio-frequency (RF) synthesizer featuring a bandwidth of 40 GHz as an electrical signal source. The RF-signal is split in two paths with a length difference of 20 cm such that the phase shift between the two drive signals can be adjusted by fine-tuning of the RF frequency. For large-signal operation with pre-distorted waveforms, an arbitrary-waveform generation (AWG) with two signal channels is used, where the waveform, output power, and phase can be individually adjusted for each channel. The bias voltages for the MZM are coupled to the chip via bias-Ts.

For our experiments, we usually chose the null point which features the lowest bias voltage. We also tried other null points without observing any relevant difference in device performance. The ends of the transmission lines are terminated with 50 Ohm to avoid spurious reflections of the electrical signal. The RF performance of our device is limited by the 50 nm thin resistive silicon slabs, the RC limitations of which can be only partly overcome by the gate voltage. There is also an impedance mismatch between the external 50 Ω drive circuit and the travelling-wave electrode of the modulator with has an impedance of only approx. 35 Ω, but this is only of minor effect. With optimized electrode design and doping profiles, significantly higher operating frequencies can be achieved [33,37,39]. For small-signal operation, sinusoidal drive signals are generated with an RF synthesizer with 40 GHz bandwidth. For the large-signal demonstration, an arbitrary-waveform generator (AWG) with 1 GHz bandwidth is used, allowing to generate arbitrarily predistorted drive signals having a fundamental frequency of at most 100 MHz and higher harmonics of at most 500 MHz. The experiments are therefore not limited by the bandwidth of the AWG. The optical output is recorded with an optical spectrum analyzer having a resolution bandwidth of 20 MHz. In a first experiment, an RF synthesizer is used to generate sinusoidal drive signals with amplitudes much smaller than the π-voltage of the MZM such that the devices are operated in the linear regime. A static gate field of 0.15 V/nm is applied between the substrate and the SOI device layer to enhance the electrical bandwidth [34], and therefore allows to use low drive voltages. The optical output spectrum for a drive signal with an angular frequency of $\Omega = 2\pi \times 0.475$ GHz is depicted in Fig. 5(a). By fine-tuning of the bias voltage, the carrier can be suppressed by 37 dB. The shifted line at $\omega_0 - \Omega$ is clearly visible with a CE of -16.4 dB and SMSR of 18.8 dB. In the experiment, the relative phase shift between both Mach-Zehnder was chosen to be $-\pi/2$, leading to the line shifted at $\omega_0 - \Omega$ instead of $\omega_0 + \Omega$ as for a $+\pi/2$ phase shift denoted above. The sign of the relative phase shift can be chosen arbitrarily, resulting only in a mirrored output spectrum. It has to be noted that the SMSR is limited by a strong spurious spectral line at $\omega \pm 2\Omega$ rather than at $\omega + 3\Omega$, as would be expected [10]. This is attributed to slightly different electro-optic coefficients of the two phase shifters in the arms of the two MZM, resulting in imperfect suppression of the even-order side lines. From the height of the side lines, we can estimate the ratio of the phase shifts of the MZM arms to be 1 : 0.8. This imbalance is attributed to the poling procedure: The MZM is poled by a applying a voltage via the floating ground electrodes of each MZM, while the center signal electrode is not contacted.

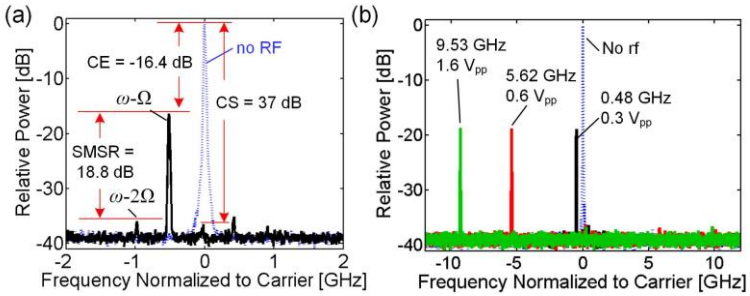

Fig. 5: Small-signal operation of the SOH frequency shifter. For reference, we also plot the unmodulated carrier obtained without RF signal and with the bias set for maximum transmission (dotted blue). This carrier not present in the output spectrum. **(a)** Modulation at $\Omega = 2\pi \times 0.475$ GHz and 0.45 V_{pp} drive voltage. The carrier suppression (CS) amounts to 37 dB, the conversion efficiency is CE = -16.38 dB and the SMSR is 18.8 dB. **(b)** Frequency shifting for different RF frequencies up to 10 GHz without degradation of the SMSR. The drive voltage is increased for higher frequencies to compensate for the decay of the modulation efficiency with frequency.

For slots with slightly different resistivities at the glass-transition temperature, this configuration may lead to slightly different poling fields hence to slightly different electro-optic coefficients. This can be overcome by applying a defined potential of $U_{poling}/2$ to the signal electrode during the poling process, which should lead to equal poling fields and hence equal electro-optic coefficients in the two slots. Another approach to overcome the issue of different electro-optic coefficients is by using dual-drive configurations of the MZM, where the modulation voltage of each phase shifter can be adjusted individually. We also demonstrate frequency shifts of up to $\Omega = 2\pi \times 10$ GHz without significant degradation of SMSR, Fig. 6(b). In these experiments, the drive voltage is increased along with the modulation frequency to compensate for the low-pass behavior of the device. Note that much higher frequency shifts can be achieved with SOH devices, for which small-signal modulation frequencies of 100 GHz have been demonstrated [40].

To increase the CE, a larger modulation depth and hence a larger drive amplitude are necessary. This leads to spurious lines in the optical spectrum, which need to be suppressed by using periodic drive signals which comprise harmonics of uneven order with carefully optimized amplitudes. These harmonics lead to a deformation of the drive signal, which, in combination with the nonlinear response of the MZM, generates approximately sinusoidal amplitude modulations at the output of each MZM. To experimentally verify this concept, we use an arbitrary waveform generator (AWG) with two channels to drive the device. Keeping the frequency at $\Omega = 2\pi \times 100$ MHz, the drive amplitude, waveform and electrical phase of each MZM can be controlled individually to minimize spurious side lines in the optical spectrum. Figure 6(a) depicts the spectrum if purely sinusoidal signals are fed to each MZM of the frequency shifter with an amplitude a_1 of approximately the π-voltage, optimized for maximum power in the $\omega_0 - \Omega$ line. This results in a CE of -4.7 dB and in an SMSR of only 16.4 dB, in good agreement with theory and with previous results in $LiNbO_3$ modulators, where a CE of -4.7 dB and an SMSR of 18.4 dB were reached [15]. We then use an experimentally optimized drive signal comprising the third and fifth harmonic, $U = a_0 \sin(\Omega t) - 0.25 \cdot a_0 \sin(3\Omega t) + 0.125 \cdot a_0 \sin(5\Omega t)$, see Fig. 6(c) for the time-domain electrical waveform. This significantly reduces the spurious side modes in the optical spectrum, Fig. 6(b). The previously dominant line at $\omega_0 + 3\Omega$, which is minimized by the third harmonic of the drive signal, is now 31 dB below the line at $\omega_0 - \Omega$.

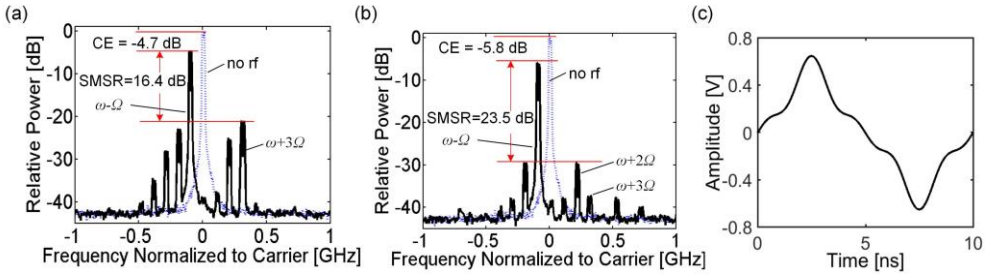

Fig. 6: The frequency shifter is driven with an AWG at an angular frequency of $\Omega = 2\pi \times 100$ MHz and a voltage of 1.3 V_{pp} at the MZM, which is optimized for maximum conversion. Each MZM of the frequency shifter is driven by a separate channel of the AWG and amplitude, phase and shape of the waveform can hence be controlled individually. **(a)** Output spectrum obtained by a pure sinusoidal drive signal, resulting in an optical spectrum with good CE but small SMSR of 16.4 dB. **(b)** Output spectrum obtained for using a drive signal with higher harmonics, which suppress the spurious lines in the optical output spectrum. By optimizing the amplitudes of the third and the fifth harmonic, the spurious component at $\omega_0 + 3\Omega$ could be reduced by over 15 dB. The overall SMSR now amounts to 23.5 dB, limited by strong spurious components at $\omega_0 \pm 2\Omega$, which are attributed to an imbalance of the phase shifters in the MZM. This can be overcome by optimized device design. Without these components, an SMSR of 31 dB could be achieved. **(c)** Waveform of the optimized drive signal for one MZM, generated by $U = a_0 \sin(\Omega t) - 0.25 \cdot a_0 \sin(3\Omega t) + 0.125 \cdot a_0 \sin(5\Omega t)$.

Note that the SMSR is again limited by the spurious lines at $\omega_0 \pm 2\Omega$, which in theory should not exist. These lines originate from the unequal efficiency of the phase shifters in the MZM, leading to an SMSR of 23.5 dB. This can be avoided by improved device design, enabling SMSR of better than 30 dB. The CE for modulation with pre-distorted signals amounts to -5.8 dB, quite close to the theoretically predicted value of - 6 dB. The fact that the theoretically predicted CE amounts to - 6 dB can be understood intuitively: For ideal compensation, the field at the output of the MZM is perfectly sinusoidal and the intensity follows a squared sinusoidal. As a consequence, half the power (3 dB) is lost on average in each of the two MZM. Moreover, the outputs of both MZM are merged with a relative phase difference of $\pi/2$ to form the single-sideband output of the IQ modulator, thereby losing again 3 dB of power. Note that this is not in contradiction to the conversion efficiency of -4.7 dB predicted and achieved for the case of large-signal modulation with sinusoidal waveform: When driving the phase modulators of the MZM with a pure sinusoidal, the field at the output of the MZM is a distorted sinusoidal, for which the average power is larger than half the peak power. As a consequence, only 1.7 dB of power is lost in each MZM, which, together with the 3 dB of loss associated with the power combiner of the outer IQ structure, leads to a theoretical CE of -4.7 dB. In summary, we can conclude that a frequency shifter with an SMSR of better than 30 dB and a CE of approximately 6 dB can be realized on the SOH platform using the SSB configuration combined with temporal shaping of the drive signal.

5. Summary and outlook

We have demonstrated for the first time a silicon-based single-sideband frequency shifter. The device is realized by SOH integration, enabling highly efficient pure phase modulation without any residual amplitude fluctuations. In small-signal operation, the device allows for broadband operation up to 10 GHz. Using large drive amplitudes along with temporal shaping of the drive signal enables a good CE of -5.8 dB while maintaining high SMSR of more than 23 dB. The SMSR can be improved further by using optimized device designs or dual-drive configurations of the modulators.

While SOH devices show already highest performance, further research is needed to improve the long-term stability of the EO materials. With the relatively low glass transition temperature of the material used here, the thermally activated reorientation of the chromophores limits the lifetime of current devices. For future device generations, the EO molecules can be modified with specific crosslinking agents. For cross-linked EO materials,

stable operation above 200 °C has already been demonstrated [41–43]. Detailed investigations on the lifetime and stability of SOH devices are currently in progress. Moreover, there is still a series of practical device-related aspects that need systematic investigation. As an example, drift of the operating point, which is well known and thoroughly investigated in $LiNbO_3$ [44] and other devices with insulating electro-optic layer, is also observed in SOH devices and requires further investigation.

Appendix

In the following section, the equations for SSB modulation are described in more detail, including temporal shaping of the drive signal. For the analysis, we assume an ideal sinusoidal amplitude transmission function for each of the MZM, which are biased in the zero-transmission point, see Fig. 2. We furthermore assume that the output signals of the two MZM are combined with a relative phase shift of π/2, corresponding to the case of an ideal IQ modulator.

The spectrum at the output of the frequency shifter as depicted in Fig. 1(a) is the coherent addition of all separate signals after the four phase modulators. The phase shift obtained for a sinusoidal drive signal at an angular frequency Ω without predistortion can be written as

$$\begin{aligned} \Phi(t) &= a_1 \sin(\Omega t) \\ \Phi'(t) &= -b_1 \cos(\Omega t), \end{aligned} \tag{2}$$

where and a_1 and b_1 represent the amplitude of the phase shift in the upper and the lower MZM, respectively. The complex optical field E at the output of the IQ modulator can then be described by

$$E = \frac{1}{4} E_0 e^{\mathrm{j}\omega_0 t} \left(e^{\mathrm{j}a_1 \sin(\Omega t)} - e^{-\mathrm{j}a_1 \sin(\Omega t)} + \mathrm{j} e^{-\mathrm{j}b_1 \cos(\Omega t)} - \mathrm{j} e^{\mathrm{j}b_1 \cos(\Omega t)} \right), \tag{3}$$

where E_0 is the amplitude and ω_0 is the frequency of the optical signal at the input. Using the Jacobi-Anger expansion for expressions of the form $e^{\mathrm{j}z\cos\theta} = \sum_{n=-\infty}^{\infty} \mathrm{j}^n J_n(z) e^{\mathrm{j}n\theta}$ and $e^{\mathrm{j}z\sin\theta} = \sum_{n=-\infty}^{\infty} J_n(z) e^{\mathrm{j}n\theta}$, where $J_n(z)$ is the n-th order Bessel function of the first kind [45], and exploiting the relation $J_n(-z) = (-1)^n J_n(z)$, Eq. (3) can be written as

$$E = \frac{1}{4} E_0 e^{\mathrm{j}\omega_0 t} \left(\begin{array}{l} \sum_{n=-\infty}^{\infty} J_n(a_1) e^{\mathrm{j}n\Omega t} - \sum_{n=-\infty}^{\infty} (-1)^n J_n(a_1) e^{-\mathrm{j}n\Omega t} \\ + \mathrm{j} \sum_{n=-\infty}^{\infty} (-\mathrm{j})^n J_n(b_1) e^{\mathrm{j}n\Omega t} - \mathrm{j} \sum_{n=-\infty}^{\infty} \mathrm{j}^n J_n(b_1) e^{-\mathrm{j}n\Omega t} \end{array} \right). \tag{4}$$

Condensing Eq. (4) for $a_1 = b_1$, the amplitude of the optical field at the output of the frequency shifter can be expressed as

$$E = E_0 \sum_{m=4n+1} J_m(a_1) e^{\mathrm{j}(\omega_0 + m\Omega)t} \quad \text{for } n \in \mathbb{Z}. \tag{5}$$

This corresponds to the output spectrum in Fig. 1(b) with lines at $\omega_0 - 3\Omega$, $\omega_0 + \Omega$, $\omega_0 + 5\Omega$ etc. For a frequency shifter, the line at $\omega_0 + \Omega$, i.e. $J_1(a_1)$, has to be maximized, which requires the amplitude a_1 of the drive signal to be close to 1.84, where the first-order Bessel function assumes a local maximum. In this regime, the higher-order Bessel function ($|m| > 7$) give no significant contribution to the output spectrum and therefore the lines at these higher frequencies can be neglected. Note that the sign of the frequency shift can be reversed by reversing the sign of the phase shift φ_Q in Fig. 1. Equation. (3) refers to $\varphi_Q = +\pi/2$; the corresponding relation for the case of $\varphi_Q = -\pi/2$ would read

$$E = \frac{1}{4} E_0 e^{\mathrm{j}\omega_0 t} \left(e^{\mathrm{j}a_1 \sin(\Omega t)} - e^{-\mathrm{j}a_1 \sin(\Omega t)} - \mathrm{j} e^{-\mathrm{j}b_1 \cos(\Omega t)} + \mathrm{j} e^{\mathrm{j}b_1 \cos(\Omega t)} \right). \tag{6}$$

In this case, the field at the output of the device is shifted towards lower frequencies,

$$E = E_0 \sum_{m=4n+1} J_m(a_1) e^{\mathrm{j}(\omega_0 - m\Omega)t} \quad \text{for } n \in \square . \tag{7}$$

To minimize the amplitudes at the spurious frequencies ω_0 - 3Ω, ω_0 + 5Ω,and ω_0 - 7Ω, a predistortion can be applied to the drive signal by introducing higher harmonics into the waveform. Exemplarily, the compensation for one spurious frequency ω_0 - 3Ω will be explained in the following. When adding the third harmonics to the electrical drive signals of the two MZM in the IQ modulator, Eq. (2) changes to

$$\begin{aligned} \Phi(t) &= a_1 \sin(\Omega t) - a_3 \sin(3\Omega t), \\ \Phi'(t) &= -b_1 \cos(\Omega t) - b_3 \cos(3\Omega t). \end{aligned} \tag{8}$$

In this relation, the quantities a_1, b_1 and a_3, b_3 represent the amplitudes of the phase shift in the upper and the lower MZM at frequencies Ω and 3Ω, respectively. This leads to phase shifts of the form

$$E = \frac{1}{4} E_0 e^{\mathrm{j}\omega_0 t} \begin{pmatrix} e^{\mathrm{j}a_1 \sin(\Omega t)} e^{-\mathrm{j}a_3 \sin(3\Omega t)} - e^{-\mathrm{j}a_1 \sin(\Omega t)} e^{\mathrm{j}a_3 \sin(3\Omega t)} \\ + \mathrm{j} e^{-\mathrm{j}b_1 \cos(\Omega t)} e^{-\mathrm{j}b_3 \cos(3\Omega t)} - \mathrm{j} e^{\mathrm{j}b_1 \cos(\Omega t)} e^{\mathrm{j}b_3 \cos(3\Omega t)} \end{pmatrix}. \tag{9}$$

The Jacobi-Anger expansion can be applied to this equation, resulting in

$$E = \frac{1}{4} E_0 e^{\mathrm{j}\omega_0 t} \begin{pmatrix} \sum_{n=-\infty}^{\infty} \sum_{k=-\infty}^{\infty} J_n(a_1) e^{\mathrm{j}n\Omega t} (-1)^k J_k(a_3) e^{\mathrm{j}k3\Omega t} \\ - \sum_{n=-\infty}^{\infty} \sum_{k=-\infty}^{\infty} (-1)^n J_n(a_1) e^{\mathrm{j}n\Omega t} J_k(a_3) e^{\mathrm{j}k3\Omega t} \\ + \mathrm{j} \sum_{n=-\infty}^{\infty} \sum_{k=-\infty}^{\infty} (-\mathrm{j})^{n+k} J_n(b_1) e^{\mathrm{j}n\Omega t} J_k(b_3) e^{\mathrm{j}k3\Omega t} \\ - \mathrm{j} \sum_{n=-\infty}^{\infty} \sum_{k=-\infty}^{\infty} \mathrm{j}^{n+k} J_n(b_1) e^{\mathrm{j}n\Omega t} J_k(b_3) e^{\mathrm{j}k3\Omega t} \end{pmatrix} \tag{10}$$

For practical applications, the modulation amplitudes a_1 and b_1 are usually smaller than 1.84, where J_1 has its maximum, and a_3 and b_3 are usually smaller than 0.5. In this regime, the dominant contributions to the four sums on the right-hand side of Eq. (10) arise from products of the form $J_0(a_1)\, J_k(a_3)$ and $J_n(a_1)\, J_0(a_3)$ that contain 0^{th}-order Bessel functions. Taking into account only these contributions, only frequency components at ω_0 + Ω, ω_0 - 3Ω, ω_0 + 5Ω ... remain in Eq. (10). Assuming further $a_1 = b_1$ and $a_3 = b_3$ and sorting by frequency components, Eq. (10) can be simplified to

$$E = E_0 e^{\mathrm{j}\omega_0 t} \begin{pmatrix} \ldots \\ + \left[\ldots + J_1(a_1) J_0(a_3) + \ldots \right] e^{\mathrm{j}\Omega t} \\ + \left[\ldots + J_{-3}(a_1) J_0(a_3) - J_0(a_1) J_{-1}(a_3) + \ldots \right] e^{-\mathrm{j}3\Omega t} \\ + \left[\ldots + J_5(a_1) J_0(a_3) + \ldots \right] e^{\mathrm{j}5\Omega t} \\ + \left[\ldots + J_{-7}(a_1) J_0(a_3) + \ldots \right] e^{-\mathrm{j}7\Omega t} \\ + \ldots \end{pmatrix}, \tag{11}$$

where the dots (…) denote expressions that either contain products of two Bessel functions of non-zero order or contributions at frequency that are outside the range [ω_0 -7Ω, ω_0 + 7Ω]. Equation (11) is equivalent to Eq. (1).

Acknowledgments

We acknowledge support by the European Research Council (ERC Starting Grant 'EnTeraPIC', number 280145), the EU-FP7 projects PHOXTROT and BigPIPES, the Alfried

Krupp von Bohlen und Halbach Foundation, the Helmholtz International Research School for Teratronics (HIRST), the Karlsruhe School of Optics and Photonics (KSOP), the Karlsruhe Nano-Micro Facility (KNMF), and by Deutsche Forschungsgemeinschaft and Open Access Publishing Fund of Karlsruhe Institute of Technology. We acknowledge financial support of The National Science Foundation (DMR-0905686, DMR- 0120967) and the Air Force Office of Scientific Research (FA9550-09-1-0682).